remote sensing

MDPI

Article

Coseismic and Postseismic Deformations of the 2023 Turkey Earthquake Doublet

Chaoya Liu [1,2], Hongru Li [1,2,*], Huili Zhan [1,2], Shaojun Wang [1,2] and Ling Bai [1,2]

[1] State Key Laboratory of Tibetan Plateau Earth System, Environment and Resources (TPESER), Institute of Tibetan Plateau Research, Chinese Academy of Sciences, Beijing 100101, China; bailing@itpcas.ac.cn (L.B.)
[2] University of Chinese Academy of Sciences, Beijing 100049, China
* Correspondence: lihongru@itpcas.ac.cn

Highlights

What are the main findings?

- The 2023 Turkey earthquake doublet exhibited a complementary spatial pattern of coseismic and postseismic fault slips, with the distribution of afterslips being influenced by the coseismic Coulomb stress changes.
- The postseismic afterslip not only compensated for the coseismic slip deficit on the deep part of the fault but also extended into previously unruptured segments during the earthquake doublet.

What are the implications of the main findings?

- These findings underscore the interplay between coseismic and postseismic processes in large strike-slip earthquakes, revealing a continuous phase of post-earthquake stress adjustment and redistribution.
- The extension of afterslip into segments adjacent to the coseismic rupture zones indicates that these fault segments are at increased risk of failure during the postseismic period and highlight the potential seismic hazard.

Abstract

On 6 February 2023, an earthquake doublet of Mw 7.8 and Mw 7.5 occurred in southeastern Turkey and caused surface ruptures over 350 km for the eastern Anatolian fault (EAF) and 150 km for the Surgu fault (SF), respectively. Over 3700 Mw > 3.0 aftershocks occurred within 5 months following the earthquake doublet, indicating that postseismic stress adjustment is evident. Here, we utilize InSAR technology to investigate the earthquake doublet in terms of its coseismic and postseismic deformations and to estimate the changes in Coulomb stress. We found that the postseismic surface deformation is consistent with the coseismic rupture, characterized by left-lateral strike-slip movement. The coseismic deformations (>5 m) are concentrated in the central-eastern (Pazarcik and Erkenek) segments in the EAF and the central (Cardak) segment in the SF. Notably, the maximum coseismic slip (up to 10 m) and the largest postseismic slip (∼0.5 m) both occurred on the Cardak segment. Postseismic deformations (>0.05 m) are concentrated in the northeastern Erkenek segment and southwestern Amanos segment of the EAF, as well as the eastern Dogansehir segment of the SF. Compared with the coseismic deformation, the postseismic slip compensated for the insufficient deeper slip of the southwestern Amanos segment of the EAF and the central Cardak segment of the SF. Additionally, the postseismic slip extended the rupture area to both the northeast of the Dogansehir segment along the SF and the epicentral area of the 2020 Mw 6.7 earthquake along the EAF. The postseismic afterslip largely reduced the potential seismic hazard of the seismic gap between the eastern end of the coseismic rupture

check for updates

Academic Editor: Angelo De Santis

Received: 31 August 2025
Revised: 3 October 2025
Accepted: 23 October 2025
Published: 29 October 2025

Citation: Liu, C.; Li, H.; Zhan, H.; Wang, S.; Bai, L. Coseismic and Postseismic Deformations of the 2023 Turkey Earthquake Doublet. *Remote Sens.* **2025**, *17*, 3573. https://doi.org/10.3390/rs17213573

Copyright: © 2025 by the authors. Licensee MDPI, Basel, Switzerland. This article is an open access article distributed under the terms and conditions of the Creative Commons Attribution (CC BY) license (https://creativecommons.org/licenses/by/4.0/).

of the 2023 Mw 7.8 earthquake and the epicentral area of the 2020 Mw 6.7 earthquake, as well as the southwestern Amanos segment of the EAF and the eastern Dogansehir segment of the SF.

Keywords: 2023 Turkey earthquake doublet; coseismic deformation; postseismic afterslip; coulomb stress

1. Introduction

On 6 February 2023, an earthquake doublet of Mw 7.8 and Mw 7.5 occurred along the East Anatolian Fault (EAF) and the nearby Surgu fault (SF) zones in Turkey (Figure 1), resulting in over 50,000 fatalities and 100,000 injuries [1]. The EAF is a major fault formed by interaction between the Anatolian subplate, the African plate, and the Arabian plate [2]. The slip rate of the EAF zone is about 10 mm/year in the northeastern segments (Puturge) and 4.5 mm/year in the southwestern segment (Amanos), indicating interseismic strain accumulation in the central (the Pazarcik and Erkenek) segment [3]. Historically large earthquakes associated with the EAF zone mainly occurred before the 20th century, and there was a seismic gap with sparse seismicity over the past 200 years [4].

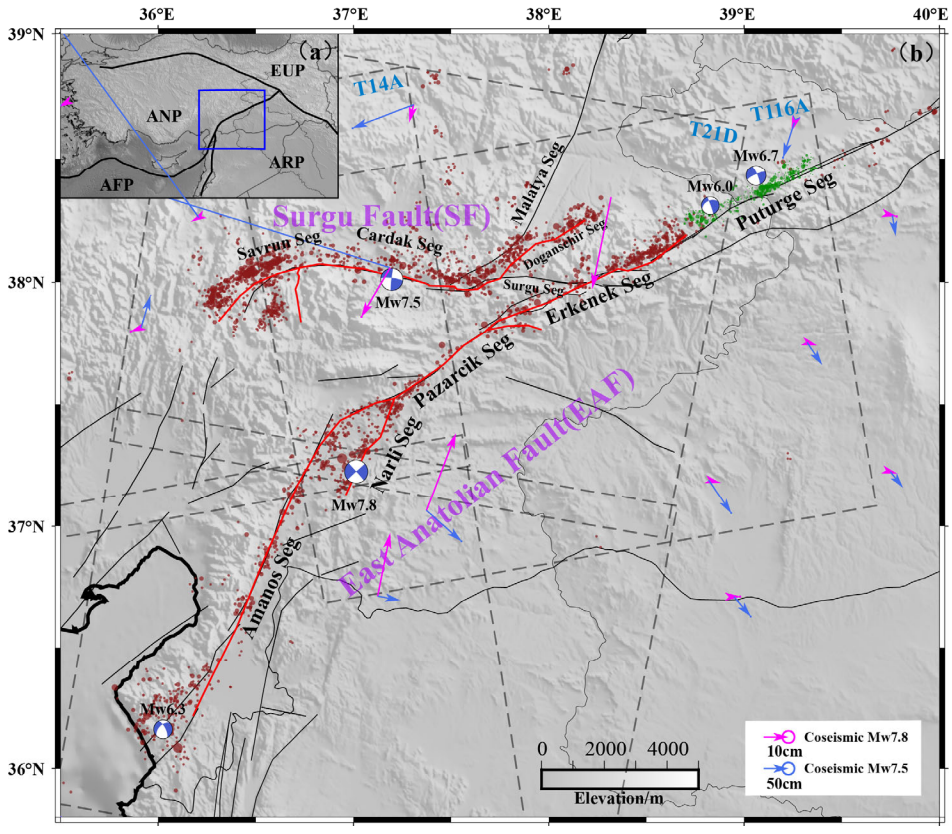


Figure 1. Tectonic setting of the 2023 Turkey earthquake doublet. (**a**) Tectonic setting of the study area, the blue box shows the region (**b**). (**b**) Blue beach balls denote the focal mechanisms of Mw 7.8, Mw 7.5, Mw 6.7, Mw 6.3, and Mw 6.0 earthquakes from the USGS (United States Geological Survey), respectively. Black and red solid lines represent faulting structures in the region and surface rupture traces caused by the 2023 earthquake doublet. Dotted lines represent satellite image coverage (ascending track T14, T116, and descending track T21). Pink and blue arrows represent the coseismic GPS displacement field [5] for Mw 7.8 and Mw 7.5 earthquakes, respectively. Brown and green dots represent aftershocks for the 2023 earthquake doublet and the 2020 Mw 6.7 earthquakes [6,7].

The coseismic rupture process of the earthquake doublet has been studied using seismic and geodetic observations. The Mw 7.8 earthquake initiated at the Narli segment and ruptured to the northeast and southwest of the EAF. The extent of the slip in the northeast (Pazarcik and Erkenek segments) along the EAF is larger than in the southwest (Amanos segment) along the EAF [6,8–11]. This along-strike variation may be attributed to the northeastward supershear rupture and dynamic stress triggering [8]. The interseismic slip rate of the central-eastern (Pazarcik, Erkenek, and Puturage) segments decreases progressively from east to west along the EAF zone [2–4]. Significant strain energy accumulation was observed in the central Pazarcik and Erkenek segments along the EAF zone. In contrast, the southwestern (Amanos) segment along the EAF likely accumulates relatively less strain energy due to its substantial deviation in fault strike direction compared to the central-eastern (Pazarcik and Erkenek) segments [2–4,10].

Coseismic Coulomb stress changes suggest that the southwestern Amanos segment experienced stress loading, indicating a higher likelihood of continued postseismic rupture. However, it remains unclear whether the Amanos segment ruptured completely during the coseismic process or if it poses a potential seismic hazard [7,11]. Additionally, the Puturge segment at the northeastern end and the Dead Sea fault at the southwestern end of the Mw 7.8 earthquake rupture zone were subjected to stress loading [12,13]. Although the surface ruptures between the northeastern end of the Mw 7.8 earthquake rupture zone and the 2020 Mw 6.7 earthquake rupture area were not spatially interconnected, the distribution of the aftershocks has bridged this gap [13,14]. This suggests that postseismic fault rupture has occurred in this region [12,15,16].

For the Mw 7.5 earthquake, the rupture was predominantly strike-slip on the SF fault, trending nearly east–west. The coseismic Coulomb stress increase produced by the Mw 7.8 earthquake at the hypocenter of the Mw 7.5 earthquake is about 0.1 MPa, which is close to the threshold of coseismic stress triggering [8]. After the Mw 7.5 earthquake, the seismicity on the central Pazarcik and Erkenek segments along the EAF is suddenly suppressed, which can be explained by the stress shadow drawn by the coseismic slip on the SF [17]. The SF experienced coseismic Coulomb stress loading at both ends and triggered aftershock clusters [13]. Compared to the central Cardak segment, the eastern Doganseshir segment exhibited a lower extent of rupture and retains the potential for rupture in the future [9,12,15,16]. As the 2023 Turkey earthquake doublet is characterized by substantial coseismic deformation and aftershock activity, it is important to investigate the postseismic stress adjustments and seismic hazards for the various segments of the EAF and the SF zones.

In this study, we utilized Sentinel-1A/B satellite data combined with the Pixel Offset Tracking (POT) technique and the PS-InSAR method to derive the coseismic and approximately 9-month postseismic deformation fields of the 2023 Turkey earthquake doublet. The coseismic deformation field incorporates range and azimuth displacements from ascending and descending orbits. We then calculated the three-dimensional (3D) coseismic deformation field from these. Based on the coseismic deformation patterns and the spatial distribution of aftershocks, we delineated the surface traces of the seismic faults and constrained the geometric configuration of the fault model. We then conducted joint inversion, incorporating both the coseismic GPS displacement and the InSAR deformation fields (Figure S1 and 2), to determine the coseismic slip distribution. In addition, we computed postseismic fault slip distributions using the postseismic deformation field. By analyzing the kinematic characteristics of faults during both the coseismic and postseismic periods, we identified a complementary relationship between the slip distributions of the two periods. Furthermore, we investigated the influence of coseismic Coulomb stress perturbations on the triggering mechanisms of afterslip and aftershocks in surrounding regions due to

coseismic Coulomb stress changes. These findings improve our understanding of seismic hazard assessments and provide new information for mitigating seismic risks for the EAF zones.

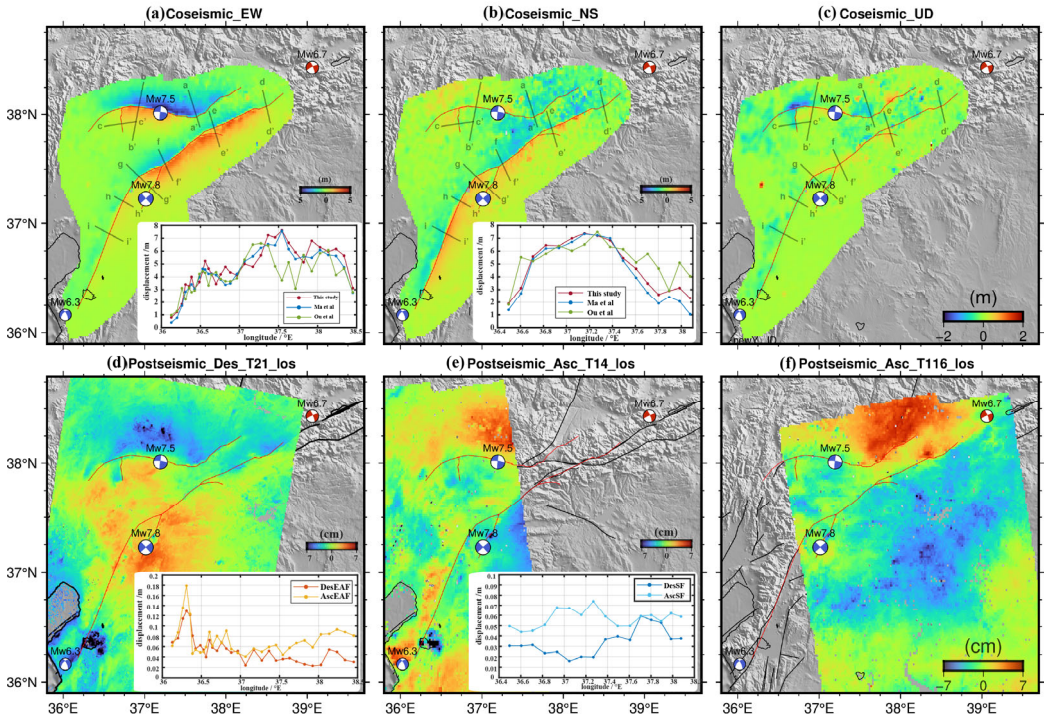


Figure 2. Analysis of the coseismic and postseismic deformation field and fault profile. The red lines represent EAF and SF, the blue beach ball represents the focal mechanism solution of the 2023 Turkey earthquake doublet. Panels (**a**–**c**) show the coseismic deformation field in the east–west, north–south, and up–down directions, Grey lines represent profiles. Panels (**d**–**f**) show the LOS deformation field of T21, T14, and T116 after the 2023 earthquake doublet. The subfigures at the lower right corner in panels (**a**,**b**) represent the relative sliding along EAF and SF in the horizontal plane. Red, blue, and green lines indicate the different results with the same way to calculate using the deformation field from this study and the previous study [18,19]. The subfigures at the lower right corner in panels d and e represent the relative sliding from ascending (light color) and descending (dark color) along EAF and SF.

2. Materials and Methods

The Sentinel-1A SAR data with interference width (IW) mode covered the deformation area of the 2023 Turkey earthquake doublet, including the descending track (T21D) and the ascending tracks (T14A and T116A) (Figure 1). As a single ascending track cannot cover the entire area of the coseismic deformation, two ascending tracks are required (Figure S1). In addition, we collected the coseismic GPS static displacement field data [5]. We calculated the GPS deformation displacement field caused by the earthquake doublet and combined it with the InSAR deformation field for the inversion. To investigate postseismic deformation, we obtained Sentinel-1A data with three tracks, similar to the coseismic data. This included 21 scenes for the T14 track with a period from 9 February 2023 to 12 November 2023, 20 scenes for the T116 track from 28 February 2023 to 7 November 2023, and 21 scenes for the T21 track from 10 February 2023 to 13 November 2023. Their reference dates are 3 June 2023, 16 July 2023, and 10 July 2023, respectively (Figure S2).

We calculated Sentinel-1A SAR image data using the ISCE (Interferometric Synthetic Aperture Radar Scientific Computing Environment, version 2.5.6) [20]. The POT (Pixel Offset Tracking) method was used to obtain the deformation field of the 2023 earthquake doublet. This analysis does cross-correlation between the SAR amplitude images after the

geometric co-registration with ISCE software and during the calculation process, precision track data is used to suppress track errors, and SRTM DEM data at a resolution of 30 m is used to eliminate topography [21]. The POT method involves analyzing SAR amplitude to measure the image distortion or offset as a small fraction of the pixel size due to the earthquake in the SAR imaging plane. This is the radar line-of-sight (LOS) (slant range) direction and the along-track (azimuth) direction parallel to the satellite motion [22,23]. Because the Sentinel-1 SLC images have very different samplings in the range (2.3 m) and azimuth (14 m) directions, we used a cross-correlation window or chip that was 64 pixels in range and 16 pixels in azimuth, or a matching window size about 150 × 220 m in size. The images were oversampled by a factor of 64 in the matching process to extract offsets with a precision of 1/64 of a pixel.

A 3D deformation field was calculated using the deformation field along the azimuth and range directions, together with the surface stress and strain model (SM) and the estimation of variance component (VCE) method (SM-VCE) [24–26]. The surrounding points are selected based on a window with adaptive size as well as the fault lines so that the 3D deformation in the near-fault zone can be obtained. Furthermore, an iterative weighted least squares method is employed to determine the relative weight of InSAR measurements within the window before the implementation of VCE.

The 3D fault geometry for the 2023 Turkey earthquake doublet was constrained through joint analysis of aftershock spatial distributions and 3D coseismic deformation fields [4,6] (Figure 3). Surface fault traces were delineated from displacements in the 3D deformation field. Fault dip angles were determined via aftershock profiles constructed perpendicular to the strike direction of the faults.

Along the SF (Figure 3a–c), the Cardak and Dogansehir segments exhibit northwest-dipping geometries (62°–80°), while the western branch shows west-dipping planes (52°–56°). Seismicity-derived dip angles align with the solutions based on InSAR [18]. However, potential contamination of aftershocks from adjacent faults [17] may yield underestimated dip estimates, contrasting with steeper angles in published SF models [8]. We therefore adopt 80° for the main SF strand and 60° for its western branch.

Along the EAF (Figure 3d–i), the Erkenek segment dips northwestward with angles increasing from 65° in the northeast to 80° in the southwest. For the Pazarcık segment, there are both northwest-dipping trends observed from coseismic InSAR deformation and southeast-dipping trends from aftershock distributions (Figure 3d–f). However, these observations consistently indicate high-angle faulting geometries (>75°) [8,17]. In contrast, the Amanos segment exhibits a southeast-dipping trend with angles increasing from 60°–82° (northeast) to 75°–83° (southwest).

The coseismic slip distribution Figure 4 of the 2023 earthquake doublet is calculated using 3D InSAR and the GPS coseismic deformation fields. The high-resolution 3D InSAR deformation field was first downsampled using a uniform sampling strategy at a fixed spatial interval to reduce computational burden while preserving the spatial integrity of the deformation signals. Guided by previously determined fault geometries, the fault planes were discretized into a series of 3 km-wide subfaults. The slip distribution on these subfaults was then estimated using the Steepest Descent Method (SDM) [27]. We use a vertically stratified and laterally homogeneous crust mode in this study. The parameters are taken from CRUST1.0. In the inversion process, we assigned equal weight (a 1:1 ratio) to the InSAR and GPS datasets. Additionally, a normalized smoothing factor of 0.2 was adopted to constrain the slip model.

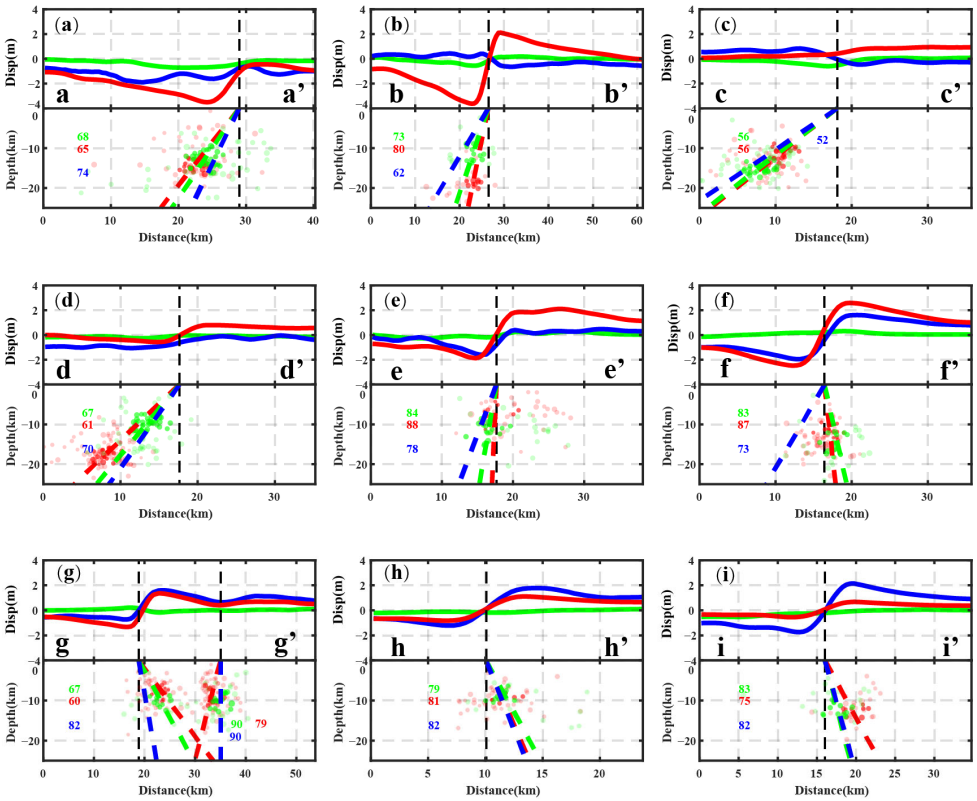


Figure 3. Profile of the 2023 earthquake doublet: coseismic deformation and aftershocks. In subfigures, red, blue, and green solid lines represent the profile value of the coseismic deformation in east–west, north–south, and up–down directions. Red and green dashed lines represent dip angle by aftershocks, which are from this study (red dot), relocated 3707 earthquakes of Mw > 3.0 within 5 months following the Mw 7.8 event [4], and other studies (green dot) relocated 2909 earthquakes of Mw > 3.0 within the first 11 days [6], respectively. Blue dashed lines represent dip angle calculated by coseismic InSAR field [18]. The letters represent the name of the profile and the locations of profiles are indicated in Figure 2. Subfigures (**a**–**c**) correspond to profiles aa′, bb′, and cc′ on the SF, respectively. Subfigures (**d**–**i**) correspond to profiles dd′, ee′, ff′, gg′, hh′, and ii′ on the EAF, respectively.

The postseismic deformation of the 2023 earthquake doublet was calculated using the reliable PS-InSAR method with approximately 9 months of InSAR data (Figures 2 and S2). First, the satellite SAR image with Single Look Complex (SLC) data in Interferometric Wide Swath (IW) mode from the Sentinel-1A satellite platform is registered using the ISCE software. Then, calculated the time series surface displacement with the Stanford Method for Persistent Scatterers InSAR (PS-InSAR) [28,29]. This technique allows nonlinear displacement signals to be detected without making any prior assumption about the deformation model [29]. Initial persistent scatterer points were filtered and merged into a grid with a size of 120 m and a standard deviation threshold of 1.5 [29]. The merged phases were then unwrapped by the 3D method [30], and the atmospheric delay error was removed using GACOS (Generic Atmospheric Correction Online Service).

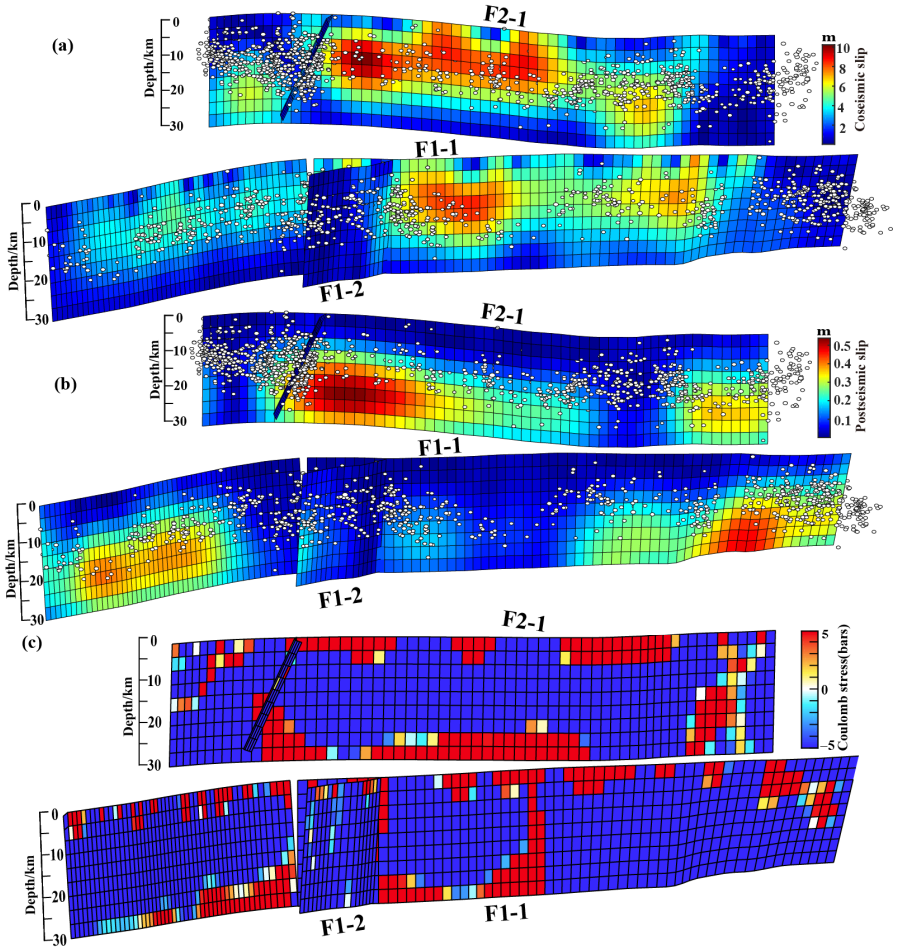


Figure 4. Coseismic and postseismic slip distribution and coseismic Coulomb stress changes in the 2023 Turkey earthquake doublet; (**a**,**b**) show the slip distributions of the coseismic and postseismic ruptures of the 2023 earthquake doublet, respectively. The white dots indicate the aftershocks of Mw > 3 within 5 months following the earthquake doublet [4]; (**c**) shows the coseismic Coulomb stress changes on the fault plane.

It is worth noting that a gap in the coseismic rupture area between the 2023 earthquake doublet and the 2020 Mw 6.7 earthquake [5], and the mutual influence of coseismic stress among them is still unclear. Therefore, we used Coulomb 3.4 software to calculate the coseismic Coulomb stress changes in four conditions: Mw 7.8, Mw 7.5, earthquake doublet, and the 2020 Mw 6.7 earthquakes. According to the 2023 earthquake doublet source mechanism solution, the receiver fault parameters were set to the same torque tensor (strike = 277°, dip = 78°, rake = 4°) as the Mw 7.5 earthquake (Figure 5a) and the same torque tensor (strike = 228°, dip = 89°, rake = −1°) as the Mw 7.8 earthquake (Figure 5b,d). The others are set to the parameter characteristics corresponding to the faults (Figure 5c). Since the influence of different effective friction coefficients on the calculated coseismic Coulomb stress change was not significant (Figure S9), we adopted a value of 0.4, following previous studies [16].

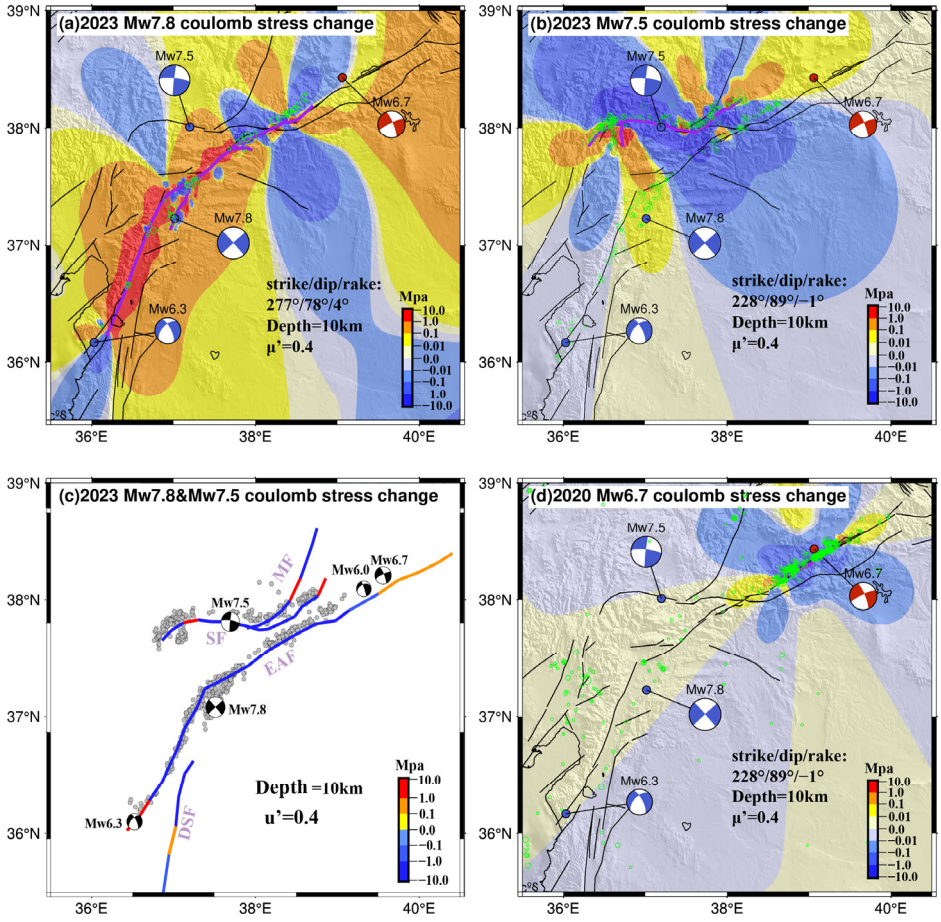


Figure 5. Coseismic Coulomb stress changes at a depth of 10 km for surrounding faults; (**a**) show the Coulomb stress change of the Mw 7.8 earthquake (Purple lines), and the green circles indicate the aftershocks that occurred before the Mw 7.5 earthquake; (**b**) show the Coulomb stress change of the Mw 7.5 earthquake (Purple lines) and aftershocks that occurred within the first 1 day after the Mw 7.5 earthquake; (**c**) show the Coulomb stress change of the 2023 earthquake doublet and aftershocks (grey Solid circles) that occurred within the first 11 days after the Mw 7.8 earthquake, the lines with different colors indicate the faults (MF: Malatya Fault, DSF: Dead Sea Fault); (**d**) show the Coulomb stress change of the 2020 Mw 6.7 earthquake and aftershocks [7].

3. Results

3.1. Coseismic Deformation and Fault Rupture

As shown in Figure 2a–c, the coseismic deformation fields of the 2023 Turkey earthquake doublet exhibit the characteristics of left-lateral strike-slip motion. Peak coseismic slips of up to 7–8 m are observed for both the EAF and SF (Figures 4a,b and S3) [31,32]. On the EAF, the northeastern (Pazarcik and Erkenek) segments show larger relative displacements (5–7 m) than the southwestern Amanos segment (3–5 m) [8]. These along-strike deformation (Figure 2) are due to changes in fault geometry, dynamic stress triggering [33].

Two prominent coseismic slip zones were identified along the EAF at the Pazarcik and Erkenek segments at depths of 5–20 km (Figure 4a). Aftershocks predominantly occurred along the edges of these primary coseismic slip zones. In contrast, the Amanos segment of the southwest EAF shows smaller coseismic slip. Aftershocks are widely distributed, suggesting incomplete coseismic rupture in the western segment [5,8,14]. Rupture propagation along the EAF terminated at the eastern end of the Erkenek segment, leaving a 40 km rupture gap between the coseismic rupture zones of the 2023 earthquake doublet and those of the 2020 Mw 6.7 earthquake. However, it seems that this coseismic rupture gap has been filled by aftershocks of the 2023 earthquake doublet (Figures 1 and 4a).

In contrast to EAF, the main rupture in SF was concentrated within the central Cardak segment with relative displacements of 5–8 m. This is much larger than the 2–4 m displacement in the eastern Dogansehir segment [31]. The western termination of the coseismic rupture in SF appears to be terminated by a branch fault, while the eastern termination appears to be controlled by a change in the strike of the fault (Figure 3a). These lateral variations in the fault segments seem to have controlled the rupture extension, with larger slip occurring in the central Cardak segment. In addition, the rupture zones in the eastern and western segments occurred at depths of 10–30 km, whereas in the central segment they occurred at depths of 0–20 km. The aftershocks in the central Cardak segment were limited and located at the deeper edge of the rupture zone. In contrast, the aftershocks in the western Savrun and eastern Dogansehir segments along the SF were more active and located at the upper edge of the rupture zones [8,10].

3.2. Postseismic Deformation and Fault Rupture

Figure 2d–f show the postseismic deformation field. The LOS deformation fields of both ascending and descending tracks exhibit left-lateral strike-slip motion. This is consistent with the coseismic deformation and indicates continued rupture propagation along the EAF and SF in the postseismic period. The postseismic deformation was primarily concentrated in two areas: the northeast of the Erkenek segment (Figure 2d,f) and the southwestern Amanos segment (Figure 2e) along the EAF. The extent of the coseismic rupture was smaller in these two areas than in the Erkenek, Cardak, and Pazarcik segments. Notably, postseismic slip in the southwestern Amanos segment along the EAF contained coseismic deformation signals from the 20 February 2023, Mw 6.3 earthquake (Figures S6 and S7), as evidenced by the progressively increasing displacement to the southwest across the fault (Figure 2d). In contrast, clear displacement extending towards the epicentral region of the 2020 Mw 6.7 earthquake is evident in the northeastern Erkenek segment along the EAF.

For the EAF, the postseismic slip distribution predominantly occurred in the downdip edge of the coseismic slip zones on the Amanos and Erkenek segments (Figures 4b and S3). The maximum value of the postseismic rupture is located in the northeast of the Erkenek segment, which is the rupture gap between the coseismic rupture zones of the Mw 7.8 earthquake and the coseismic slip area of the 2020 Mw 6.7 earthquake. The postseismic slip appears to have primarily occurred in the deeper portions of the EAF (10–30 km depth), particularly at the northeastern and southwestern ends. This is complementary to the for the predominant occurrence of coseismic slip at the central and shallow part of the EAF (0–20 km depth).

Postseismic slip in the SF is primarily concentrated in the central Cardak and eastern Dogansehir segments (Figures 2 and S5). Compared to the coseismic deformation, the postseismic deformation in the Dogansehir segment exhibits a clear northeastward extension (Figure 2d,f). Notably, the Dogansehir segment of the SF and the Erkenek segment of the EAF share a similar NE-SW direction, with their postseismic ruptures propagating in a northeastward direction. This kinematic linkage may reflect tectonic coupling with strain energy accumulation along the NE-SW propagation direction of the EAF during the interseismic period.

Postseismic slip distribution in the SF reveals that the largest afterslip of about 0.5 m occurred at the deeper depth at the central Cardak segment below the coseismic rupture zone (Figures 4 and S3). Meanwhile, the eastern Dogansehir segment exhibits horizontal complementarity, with postseismic slip extending horizontally beyond the margin of coseismic rupture. Specifically, the postseismic afterslip of the Cardak segment is concentrated at a depth of 15–25 km, underlying the shallow coseismic slip zone (0–15 km). This suggests that the postseismic slip diffused downward due to coseismic stress. The Dogansehir

segment (Figure 4a), which is subparallel to the Erkenek segment, shows limited coseismic rupture but significant aftershock activity [5,13]. This indicates that there is continued postseismic rupture propagation along these two parallel structures.

3.3. Coseismic Coulomb Stress Change

Pronounced slip complementarity is observed between coseismic and postseismic in the fault slip distribution (Figure 4a,b), similar to that observed in the 2021 Maduo earthquake [14]. Coseismic slip typically induces stress amplification along the margins of the main rupture zone, which can lead to subsequent postseismic stress release. In order to investigate the interplay between the coseismic and postseismic processes, we calculated Coulomb stress changes induced by the 2023 Turkey earthquake doublet for their fault planes (Figure 4c). On the fault planes, the coseismic Coulomb stress changes exhibits clear stress shadows (unloading) within the main rupture zones, with stress loading concentrated at the downdip extensions and edges of the main rupture zones along strike. Along the EAF, significant coseismic Coulomb stress loading occurs at a depth of 20–30 km in the Amanos and Pazarcik segments (Figure 4c). However, the postseismic slip zones in the Erkenek segment correlate with stress shadows, reflecting partial stress release in coseismic rupture. Residual stresses in these areas likely drove continued afterslip. The southwestern Amanos segment shows coseismic Coulomb stress loading at the downdip edge of the coseismic rupture zone, whereas the nearby Narli segment of the EAF exhibits dominantly unloading patterns.

While the EAF generally follows the expected Coulomb stress changes and slip relationship (coseismic Coulomb stress loading zones corresponding to postseismic afterslip), there are some discrepancies: afterslip has occurred in regions where there is a coseismic stress shadow. This complexity may arise from heterogeneous fault geometry, distributed slip patches, and spatially variable rake angles. Strike-specific contrasts emerge between the earthquake doublet: The Mw 7.5 earthquake demonstrates clearer stress-slip coupling, with stress loading concentrated at the downdip edge and northeastern extension of the coseismic rupture zone. This is consistent with the postseismic slip distribution. In contrast, the Mw 7.8 event exhibits less spatially coherent stress-slip correlations, likely due to its more distributed rupture geometry and stronger interactions with geometric complexities. This contrast highlights the way in which fault maturity and geometric heterogeneity modulate stress transfer efficiency.

The coseismic Coulomb stress changes for the surrounding faults (Figures 5a and S8) indicate a clear relationship between stress loading and triggering of the 2023 earthquake doublet. This is consistent with other previous studies [9,12,15,16]. Additionally, coseismic Coulomb stress loading is evident in the northeastern extension of the Erkenek segment and the southwestern Amanos segment. These regions have substantial aftershocks, pronounced surface deformation, and postseismic fault rupture phenomena. Notably, on 20 February 2023, an Mw 6.3 earthquake occurred in the southwestern end of the Amanos segment (Figure S8). The Mw 7.5 earthquake induced Coulomb stress loading at both ends of the SF with substantial aftershocks in postseismic (Figure 5b). Integrated analysis of the 2023 earthquake doublet (Figure 5c) reveals stress loading in three primary areas: the southwestern Amanos segment and northeastern Erkenek segment of the EAF, the eastern segment of the SF. These stress loading zones likely drove the significant postseismic surface displacements observed in these regions. Furthermore, the coseismic Coulomb stress changes from the 2020 Mw 6.7 earthquake (Figure 5d) show limited stress loading (ΔCFS < 0.1 MPa) in the southwestern part of its coseismic rupture. This may suggest that there was insufficient stress accumulation to trigger large subsequent events on the scale of the 2023 earthquake doublet.

4. Discussion

4.1. Comparison of Coseismic Slip Models

We compare the results of different coseismic slip models in terms of fault geometry, slip magnitude, and distribution. Early coseismic slip models assumed a single fault dip and a simple segment [11]. However, combined with the geodetic and aftershock data, it shows that the fault strike and dip variations are more complex. Consequently, models reflecting fault segment variations are required. We compare several typical fault models, including calculations from geodetic and aftershock data, respectively [9,17,18]. While the main trends in the fault geometries calculated from the InSAR field or aftershock data are similar, there are also obvious differences in individual segments (Figures 4 and S3). It is possible that the coseismic deformation includes the effects of events other than the 2023 earthquake doublet, such as aftershocks or landslides.

It is possible that the computational methods for deriving fault geometries from InSAR data could fail to yield a definitive solution, or that the aftershocks include seismic events on other branch faults. Combining the results of multiple fault geometries can determine the main fault geometry, providing a more accurate fault model for acquiring fault slip distribution. The maximum slip (~7–8 m) located in the Pazarcik segment of the EAF is slightly smaller than the maximum slip (~8–10 m) in the Cardak segment of the SF [5,6,9–11,14,17,18]. Some studies suggest that the maximum slip in the EAF may exceed 8 m [9–11]. The discrepancy in the estimated maximum slip on the Surgu Fault (SF) arises primarily from variations in the datasets and fault models used.

4.2. Coseismic and Postseismic Interactions

Comparison of the slip distributions of the 2023 earthquake doublet between the coseismic and postseismic processes (Figures 4 and S3) reveals that the postseismic slip mainly occurred at the down-dip edge of the coseismic rupture region on the fault plane, extending to both ends of the faults. This complementary relationship between coseismic and postseismic fault slip distributions is also found in other strike-slip earthquakes. For example, the postseismic slip of the 2001 Mw 7.8 Kunlun earthquake [34] and the 2010 Mw 6.9 Yushu earthquake [35] was randomly distributed in both the up-dip and down-dip directions of the coseismic rupture on the fault plane. However, the postseismic afterslip of the 2004 Mw 6.0 Parkfield strike-slip earthquake mainly occurred in the up-dip direction of the coseismic rupture. The peak postseismic afterslip (0.3 m) of the 2021 Mw 7.4 Mado earthquake accounts for ~6% of the maximum coseismic slip (5 m) on fault plane. This ratio is comparable to that observed in the 2023 Turkey earthquake doublet, where the afterslip (0.5 m) constituted ~5% of the maximum coseismic slip (10 m) on fault plane.

The three main sources of postseismic deformation are seismic afterslip, viscoelastic relaxation, and pore rebound [36]. Many studies have attributed deformation in the days to months after an earthquake to postseismic afterslip [37,38]. The postseismic deformation field suggests that fault rupture extends to the surface surrounding the fault and predicted surface displacements due to viscoelastic relaxation 270 days after the 2023 Turkey earthquake doublet is not signification (0.05 m). Therefore, postseismic afterslip is more likely to be the process by which coseismic stress drives short-term postseismic fault slip. Comparison of the relationship between postseismic afterslip and coseismic Coulomb stress changes (Figures 4, 5, S3 and S8) suggests that afterslip occurs mainly in the region of increased Coulomb stress, suggesting the 2023 earthquake doublet generates a stress-driven afterslip. This result is in agreement with the physics-based assumption of the stress-driven afterslip model, in which the increased stress driven by coseismic slip should be subsequently released aseismically [39]. Most aftershocks are mainly located in the edges of the coseismic rupture, which is similar to the 2021 Mw 7.4 Mado earthquake [40].

4.3. Fault Rupture Process and Potential Risk from Surrounding Faults

The coseismic rupture of the Mw 7.8 earthquake is characterized by two main slip asperities along the EAF. The ruptures of the Pazarcik and Erkenek segments are larger than those of the southwestern Amanos segment [5,6,14,16,41,42]. The coseismic fault rupture of the Mw 7.8 earthquake originated at the Narli fault. Subsequently, dynamic stress propagated northeast direction, triggering the rupture to extend in the northeastern (Pazarcik and Erkenk) segment and southwestern (Amanos) segment along the EAF. The Narli segment has a similar strike of NE-SW as the Pazarcik and Erkenk segments in EAF. This may help explain why the northeastern segment of the EAF experienced higher rupture velocities and greater slip magnitudes than the southwestern segment [8,43]. In comparison, the interseismic slip rate of the entire EAF zone decreases from northeast to southwest [8,9], due to the change in fault strike and in dip angle. Consequently, the interseismic strain energy accumulation is higher in the Pazarcik and Erkenk segments, hindering the transfer of strain energy to the Amanos segment [8]. Another possible reason is that the coseismic Coulomb stress change in historical earthquakes in the region loaded the Pazarcik segment and unloaded the Amanos segment [43]. After the 2023 Turkey earthquake doublet, the southwestern end of the Amanos segment was subjected to stress-loading and triggered the Mw 6.3 earthquake. Coulomb stress transfer also loaded the nearby Dead Sea Fault [43], significantly increasing its risk of generating future seismicity [9,12,15].

The close spatiotemporal correlation between the 2023 earthquake doublet suggests a causal relationship [17]. Through many well-documented seismic cases, such as the Nepal earthquake sequence of Mw 7.8 and Mw 7.3 occurred in 2015 [44], the triggering mechanisms between medium and large earthquake sequences have been widely explored. Many scholars both in China and abroad calculated the Mw 7.8 earthquake with Coulomb stress change, showing that the Mw 7.8 earthquake has a significant trigger relationship for Mw 7.5 events, and several aftershock groups also appeared in the Coulomb stress loading area (Figure 5a). The coseismic rupture of the Mw 7.5 earthquake at the SF shows a large rupture zone in the central segment and a lower rupture zone at both ends. The rupture propagation may be terminated by the Savrun segment due to branching faults. The near-parallel strike of the Dogansheir and Erkenek segments appears to jointly unload interseismic strain energy from the eastern part of the EAF. This may suggest that the internal secondary faults parallel to the plate boundary faults have a high risk of seismicity [43].

In addition, both faults are subject to postseismic stress loading, postseismic afterslip, and rupture extension. In particular, there is a rupture gap along the EAF between the eastern end of coseismic rupture of the Mw 7.8 earthquake and the coseismic rupture of the 2020 Mw 6.7 earthquake [5,13]. Although postseismic afterslip compensates for the rupture gap and releases some of the strain energy, the rupture extent of the 2023 earthquake doublet along the EAF is much greater than the 2020 Mw 6.7 earthquake. With the postseismic Coulomb stress loading in the northeast of the Erkenek segment, postseismic afterslip has propagated to the Puturge segment, which is located near the epicenter of the 2020 Mw 6.7 earthquake. An Mw 6.0 earthquake occurred on 16 October 2024, located at the rupture zone between the 2023 earthquake doublet and the 2020 Mw 6.7 earthquake, indicating the risk of seismicity in the postseismic afterslip region.

5. Conclusions

We used InSAR measurements to study the coseismic 3D deformation and postseismic deformation within 9 months of the 2023 Turkey earthquake doublet. The postseismic deformation is characterized by left-lateral strike-slip motion, consistent with the coseismic deformation. The coseismic fault rupture was concentrated in the Pazarcik and Erkenek

segments of the EAF and in the Cardak segment of the SF. This phenomenon is likely linked to systematic along-strike variations in fault geometry. Notably, the central (Cardak) segment of the SF displays a predominant E-W direction, whereas its terminal (Savrun and Dogansehir) segments transition toward a NE-SW direction. Similarly, along the EAF, the strike direction rotates progressively from NE-SW in the northeast to nearly N-S in the southwest.

The fault geometry was characterized by the surface trace position and dip angle. For the 2023 earthquake doublet, the fault trace was constrained using the 3D coseismic deformation field, while the dip angle was derived from the distribution of aftershocks and the surface fault trace. By integrating these results with existing fault models, a comprehensive 3D fault model was developed. This model reveals a variation in dip angle along the Erkenek segment and a change in strike direction between the Pazarcık and Amanos segments in the EAF. The existence of branch fault, stress dynamic transmission trigger influence, variation in strike direction, and so on may cause fault rupture to present segment characteristics [8]. During the postseismic period, regions including both termini of the EAF and SF, as well as the Amanos segment of the EAF, experienced increased Coulomb stress. This is evidenced by frequent aftershocks and significant afterslip, indicating sustained postseismic activity in these areas.

The postseismic afterslip not only compensates for coseismic slip deficits spatially but also facilitates along-strike rupture propagation. The Amanos segment is affected by the coseismic Coulomb stress loading, and the postseismic afterslip is obvious, which compensates for coseismic slip deficits and the deeper part of the coseismic rupture. The southwestern Dead Sea fault is also loaded by stress, which should receive more attention.

In addition, the northeast of both the Dogansheir segment and Erkenek segment continues to rupture, extending to the epicentral area of the 2020 Mw 6.7 earthquake along the EAF, so postseismic afterslip compensates for the rupture gap and releases some of the strain energy. On 16 October 2024, a Mw 6.0 earthquake occurred in this rupture gap, indicating that the regional faults by the 2023 earthquake doublet coseismic Coulomb stress loading were activated and appeared to rupture. This suggests that the risk of seismicity in postseismic areas cannot be ignored and should be given more attention.

Supplementary Materials: The following supporting information can be downloaded at: https://www.mdpi.com/article/10.3390/rs17213573/s1, Figure S1: Coseismic InSAR deformation field of the 2023 Turkey earthquake doublet;. Figure S2: Spatio-temporal baseline of the postseismic ascending (T14 and T116) and desending (T21) PS-InSAR Time series; Figure S3: Slip distribution of the Coseismic, postseismic, and Coulomb stress change on the fault plane; Figure S4: The observations, simulations, and residuals of the coseismic 3D InSAR deformation field; Figure S5: The observations, simulations, and residuals of the postseismic InSAR observations; Figure S6: The slip distribution of the Mw 6.3 earthquake on February 20, 2023; Figure S7: The InSAR observations, simulations, and residuals of the coseismic Mw 6.3 earthquake; Figure S8: The disturbances to the surrounding faults caused by the coseismic Coulomb stress changes of the 2023 Turkey earthquake doublet at different depths (5 km, 10 km, 15 km, 20 km); Figure S9: The coseismic Coulomb stress change of the Mw 7.5 earthquake; Figure S10: Predicted surface displacements due to viscoelastic relaxation 270 days after the 2023 Turkey earthquake doublet.

Author Contributions: Conceptualization, C.L. and L.B.; methodology, C.L. and S.W.; software, C.L. and S.W.; validation, H.L., L.B. and C.L.; formal analysis, C.L.; investigation, C.L.; resources, H.Z.; data curation, C.L.; writing—original draft preparation, C.L.; writing—review and editing, C.L., L.B., H.Z. and H.L.; visualization, C.L. and S.W.; supervision, L.B.; project administration, L.B.; funding acquisition, L.B. All authors have read and agreed to the published version of the manuscript.

Funding: This research is supported by the grants of the National Nature Science Foundation of China (No. 42130312).

Data Availability Statement: The original contributions presented in the study are included in the article/Supplementary Materials, further inquiries can be directed to the corresponding author.

Acknowledgments: The Sentinel-1 SAR data were downloaded from the Alaska website (https://search.asf.alaska.edu/, accessed on 24 February 2023) and were retrieved from the Alaska Satellite Facility Distributed Active Archive Center (https://vertex.daac.asf.alaska.edu, accessed on 24 February 2023). The figures were made using free GMT (Generic Mapping Tools, version 6.4) software. The coseismic fault slip distribution was inverted using the SDM software (https://github.com/RongjiangWang/SDM, accessed on 20 January 2023). We thank the editor and the four anonymous reviewers for their constructive suggestions that significantly improved the quality of the manuscript.

Conflicts of Interest: The authors declare no conflicts of interest.

References

1. Hussain, E.; Kalaycioglu, S.; Milliner, C.W.D.; Cakir, Z. Preconditioning the 2023 Kahramanmaras (Turkiye) earthquake disaster. *Nat. Rev. Earth Environ.* **2023**, *4*, 287–289. [CrossRef]
2. Hatzfeld, D.; Molnar, P. Comparisons of the kinematics and deep structures of the Zagros and Himalaya and of the Iranian and Tibetan plateaus and geodynamic implications. *Rev. Geophys.* **2010**, *48*, 2. [CrossRef]
3. Aktug, B.; Ozener, H.; Dogru, A.; Sabuncu, A.; Turgut, B.; Halicioglu, K.; Yilmaz, O.; Havazli, E. Slip rates and seismic potential on the East Anatolian Fault System using an improved GPS velocity field. *J. Geodyn.* **2016**, *94–95*, 1–12. [CrossRef]
4. Zhan, H.; Bai, L.; Adi Wibowo, B.; Liu, C.; Oike, K.; Ishikawa, Y. The 2023 Turkey earthquake doublet: Earthquake relocation, seismic tomography, and stress field inversion. *Earth Planet. Phys.* **2024**, *8*, 535–548. [CrossRef]
5. Barbot, S.; Luo, H.; Wang, T.; Hamiel, Y.; Piatibratova, O.; Javed, M.T.; Braitenberg, C.; Gurbuz, G. Slip distribution of the February 6, 2023 M_w 7.8 and M_w 7.6, Kahramanmaraş, Turkey earthquake sequence in the East Anatolian fault zone. *Seismica* **2023**, *2*, 502. [CrossRef]
6. Melgar, D.; Taymaz, T.; Ganas, A.; Crowell, B.; Öcalan, T.; Kahraman, M.; Tsironi, V.; Yolsal-Çevikbil, S.; Valkaniotis, S.; Irmak, T.S.; et al. Sub- and super-shear ruptures during the 2023 M_w 7.8 and M_w 7.6 earthquake doublet in SE Türkiye. *Seismica* **2023**, *2*, 3. [CrossRef]
7. Konca, A.Ö.; Karabulut, H.; Güvercin, S.E.; Eskiköy, F.; Özarpac, S.; Özdemir, A.; Floyd, M.; Ergintav, S.; Dogan, U. From Interseismic Deformation With Near-Repeating Earthquakes to Co-Seismic Rupture: A Unified View of the 2020 M6.8 Sivrice (Elazig) Eastern Turkey Earthquake. *J. Geophys. Res. Solid Earth* **2021**, *126*, 10. [CrossRef]
8. Ren, C.; Wang, Z.; Taymaz, T.; Hu, N.; Luo, H.; Zhao, Z.; Yue, H.; Song, X.; Shen, Z.; Xu, H.; et al. Supershear triggering and cascading fault ruptures of the 2023 Kahramanmaras, Turkiye, earthquake doublet. *Science* **2024**, *383*, 305–311. [CrossRef]
9. Liu, C.; Lay, T.; Wang, R.; Taymaz, T.; Xie, Z.; Xiong, X.; Irmak, T.S.; Kahraman, M.; Erman, C. Complex multi-fault rupture and triggering during the 2023 earthquake doublet in southeastern Turkiye. *Nat. Commun.* **2023**, *14*, 5564. [CrossRef]
10. Jia, Z.; Jin, Z.; Marchandon, M.; Ulrich, T.; Gabriel, A.A.; Fan, W.; Shearer, P.; Zou, X.; Rekoske, J.; Bulut, F.; et al. The complex dynamics of the 2023 Kahramanmaras, Turkey, M_w 7.8–7.7 earthquake doublet. *Science* **2023**, *381*, 985–990. [CrossRef]
11. Xu, J.; Liu, C.L.; Xiong, X. Source Process of the 24 January 2020 6.7 East Anatolian Fault Zone, Turkey, Earthquake. *Seismol. Res. Lett.* **2020**, *91*, 3120–3128. [CrossRef]
12. Zhao, J.-J.; Chen, Q.; Yang, Y.-H.; Xu, Q. Coseismic Faulting Model and Post-Seismic Surface Motion of the 2023 Turkey–Syria Earthquake Doublet Revealed by InSAR and GPS Measurements. *Remote Sens.* **2023**, *15*, 3327. [CrossRef]
13. Wang, W.; Liu, Y.; Fan, X.; Ma, C.; Shan, X. Coseismic Deformation, Fault Slip Distribution, and Coulomb Stress Perturbation of the 2023 Türkiye-Syria Earthquake Doublet Based on SAR Offset Tracking. *Remote Sens.* **2023**, *15*, 5443. [CrossRef]
14. He, L.; Feng, G.; Xu, W.; Wang, Y.; Xiong, Z.; Gao, H.; Liu, X. Coseismic Kinematics of the 2023 Kahramanmaras, Turkey Earthquake Sequence From InSAR and Optical Data. *Geophys. Res. Lett.* **2023**, *50*, 17. [CrossRef]
15. Dai, X.; Liu, X.; Liu, R.; Song, M.; Zhu, G.; Chang, X.; Guo, J. Coseismic slip distribution and Coulomb stress change of the 2023 M_w 7.8 Pazarcik and M_w 7.5 Elbistan earthquakes in Turkey. *Remote Sens.* **2024**, *16*, 240. [CrossRef]
16. Li, S.; Wang, X.; Tao, T.; Zhu, Y.; Qu, X.; Li, Z.; Huang, J.; Song, S. Source model of the 2023 Turkey earthquake sequence imaged by sentinel-1 and GPS measurements: Implications for heterogeneous fault behavior along the East Anatolian Fault Zone. *Remote Sens.* **2023**, *15*, 2618. [CrossRef]
17. Ding, H.; Zhou, Y.; Ge, Z.; Taymaz, T.; Ghosh, A.; Xu, H.; Irmak, T.S.; Song, X. High-resolution seismicity imaging and early aftershock migration of the 2023 Kahramanmaraş (SE Türkiye) M_w 7.9 & 7.8 earthquake doublet. *Earthq. Sci.* **2023**, *36*, 417–432. [CrossRef]

18. Ma, Z.; Li, C.; Jiang, Y.; Chen, Y.; Yin, X.; Aoki, Y.; Yun, S.H.; Wei, S. Space Geodetic Insights to the Dramatic Stress Rotation Induced by the February 2023 Turkey—Syria Earthquake Doublet. *Geophys. Res. Lett.* **2024**, *51*, e2023GL107788. [CrossRef]
19. Nergizci, M.; Lazecky, M.; Ou, Q.; Wright, T.; Hooper, A. Along-Track Displacement of M_w 7.8 and 7.6 Kahramanmaraş Earthquakes from Sentinel-1 Offset Tracking and Burst Overlap Interferometry. *Procedia Comput. Sci.* **2024**, *239*, 2135–2141. [CrossRef]
20. Rosen, P.A.; Gurrola, E.; Sacco, G.F.; Zebker, H. The InSAR scientific computing environment. In Proceedings of the EUSAR 2012; 9th European Conference on Synthetic Aperture Radar, Nuremberg, Germany, 23–26 April 2012; pp. 730–733. Available online: https://ieeexplore.ieee.org/document/6217174 (accessed on 23 October 2025).
21. Gao, Y.; Wang, K.; Liu, X. Exploitation of SRTM DEM in InSAR data processing and its application to phase unwrapping. *J. Electromagn. Waves Appl.* **2012**, *26*, 1788–1797. [CrossRef]
22. Simons, M.; Fialko, Y.; Rivera, L. Coseismic deformation from the 1999 M_w 7.1 Hector Mine, California, earthquake as inferred from InSAR and GPS observations. *Bull. Seismol. Soc. Am.* **2002**, *92*, 1390–1402. [CrossRef]
23. Pathier, E.; Fielding, E.J.; Wright, T.J.; Walker, R.; Parsons, B.E.; Hensley, S. Displacement field and slip distribution of the 2005 Kashmir earthquake from SAR imagery. *Geophys. Res. Lett.* **2006**, *33*, 20. [CrossRef]
24. Liu, J.H.; Hu, J.; Li, Z.W.; Zhu, J.J.; Sun, Q.; Gan, J. A Method for Measuring 3-D Surface Deformations With InSAR Based on Strain Model and Variance Component Estimation. *IEEE Trans. Geosci. Remote Sens.* **2018**, *56*, 239–250. [CrossRef]
25. Liu, J.; Hu, J.; Xu, W.; Li, Z.; Zhu, J.; Ding, X.; Zhang, L. Complete three—Dimensional coseismic deformation field of the 2016 Central Tottori earthquake by integrating left—And right—Looking InSAR observations with the improved SM—VCE method. *J. Geophys. Res. Solid Earth* **2019**, *124*, 12099–12115. [CrossRef]
26. Liu, J.; Hu, J.; Li, Z.; Ma, Z.; Wu, L.; Jiang, W.; Feng, G.; Zhu, J. Complete three-dimensional coseismic displacements due to the 2021 Maduo earthquake in Qinghai Province, China from Sentinel-1 and ALOS-2 SAR images. *Sci. China Earth Sci.* **2022**, *65*, 687–697. [CrossRef]
27. Wang, Y.; Wang, M.; Shen, Z.-K.; Ge, W.; Wang, K.; Wang, F.; Sun, J. Inter-seismic deformation field of the Ganzi-Yushu fault before the 2010 M_w 6.9 Yushu earthquake. *Tectonophysics* **2013**, *584*, 138–143. [CrossRef]
28. Hooper, A.; Bekaert, D.; Spaans, K.; Arıkan, M. Recent advances in SAR interferometry time series analysis for measuring crustal deformation. *Tectonophysics* **2012**, *514–517*, 1–13. [CrossRef]
29. Hooper, A.; Segall, P.; Zebker, H. Persistent scatterer interferometric synthetic aperture radar for crustal deformation analysis, with application to Volcán Alcedo, Galápagos. *J. Geophys. Res. Solid. Earth* **2007**, *112*, B7. [CrossRef]
30. Hooper, A.; Zebker, H. Phase unwrapping in three dimensions with application to InSAR time series. *J. Opt. Soc. Am. A* **2007**, *24*, 2737–2747. [CrossRef]
31. Karabulut, H.G.; Güvercin, S.E.; Hollingsworth, J.; Konca, A.Ö. Long silence on the East Anatolian Fault Zone (Southern Turkey) ends with devastating double earthquakes (6 February 2023) over a seismic gap: Implications for the seismic potential in the Eastern Mediterranean region. *Geol. Soc. Lond.* **2023**, *180*, 3. [CrossRef]
32. Karabacak, V.; Özkaymak, Ç.; Sözbilir, H.; Tatar, O.; Aktuğ, B.; Özdağ, Ö.C.; Çakir, R.; Aksoy, E.; Koçbulut, F.; Softa, M. The 2023 Pazarcık (Kahramanmaraş, Türkiye) earthquake (M_w 7.7): Implications for surface rupture dynamics along the East Anatolian fault zone. *J. Geol. Soc.* **2023**, *180*, 3. [CrossRef]
33. Liu, J.; Huang, C.; Zhang, G.; Shan, X.; Korzhenkov, A.; Taymaz, T. Immature characteristics of the East Anatolian Fault Zone from SAR, GNSS and strong motion data of the 2023 Turkiye-Syria earthquake doublet. *Sci. Rep.* **2024**, *14*, 10625. [CrossRef]
34. Wen, Y.; Li, Z.; Xu, C.; Ryder, I.; Bürgmann, R. Postseismic motion after the 2001 MW 7.8 Kokoxili earthquake in Tibet observed by InSAR time series. *J. Geophys. Res. Solid Earth* **2012**, *117*, B8. [CrossRef]
35. Zhang, G.; Shan, X.; Feng, G. The 3-D surface deformation, coseismic fault slip and after-slip of the 2010 M_W 6.9 Yushu earthquake, Tibet, China. *J. Asian Earth Sci.* **2016**, *124*, 260–268. [CrossRef]
36. He, L.; Feng, G.; Wu, X.; Lu, H.; Xu, W.; Wang, Y.; Liu, J.; Hu, J.; Li, Z. Coseismic and Early Postseismic Slip Models of the 2021 Mw 7.4 Maduo Earthquake (Western China) Estimated by Space-Based Geodetic Data. *Geophys. Res. Lett.* **2021**, *48*, e2021GL095860. [CrossRef]
37. Liu, S.; Shen, Z.-K.; Bürgmann, R.; Jónsson, S. Thin crème brûlée rheological structure for the Eastern California Shear Zone. *Geology* **2020**, *49*, 216–221. [CrossRef]
38. Liu, X.; Xu, W. Logarithmic Model Joint Inversion Method for Coseismic and Postseismic Slip: Application to the 2017 M_w 7.3 Sarpol Zahāb Earthquake, Iran. *J. Geophys. Res. Solid Earth* **2019**, *124*, 12034–12052. [CrossRef]
39. Sreejith, K.M.; Sunil, P.S.; Agrawal, R.; Saji, A.P.; Ramesh, D.S.; Rajawat, A.S. Coseismic and early postseismic deformation due to the 25 April 2015, M 7.8 Gorkha, Nepal, earthquake from InSAR and GPS measurements. *Geophys. Res. Lett.* **2016**, *43*, 3160–3168. [CrossRef]
40. Johnson, K.M.; Burgmann, R.; Larson, K. Frictional properties on the San Andreas fault near Parkfield, California, inferred from models of afterslip following the 2004 earthquake. *Bull. Seismol. Soc. Am.* **2006**, *96*, S321–S338. [CrossRef]

41. An, Q.; Feng, G.; He, L.; Xiong, Z.; Lu, H.; Wang, X.; Wei, J. Three-dimensional deformation of the 2023 Turkey M_w 7.8 and M_w 7.7 earthquake sequence obtained by fusing optical and SAR images. *Remote Sens.* **2023**, *15*, 2656. [CrossRef]
42. Xu, L.; Aoki, Y.; Wang, J.; Cui, Y.; Chen, Q.; Yang, Y.; Yao, Z. The 2023 M_w 7.8 and 7.6 earthquake doublet in Southeast Türkiye: Coseismic and early postseismic deformation, faulting model, and potential seismic hazard. *Seismol. Res. Lett.* **2024**, *95*, 562–573. [CrossRef]
43. Chen, J.; Liu, C.; Dal Zilio, L.; Cao, J.; Wang, H.; Yang, G.; Göğüş, O.H.; Zhang, H.; Shi, Y. Decoding stress patterns of the 2023 Türkiye—Syria earthquake doublet. *J. Geophys. Res. Solid Earth* **2024**, *129*, 10. [CrossRef]
44. Bai, L.; Klemperer, S.L.; Mori, J.; Karplus, M.S.; Ding, L.; Liu, H.; Li, G.; Song, B.; Dhakal, S. Lateral variation of the Main Himalayan Thrust controls the rupture length of the 2015 Gorkha earthquake in Nepal. *Sci. Adv.* **2019**, *5*, eaav0723. [CrossRef] [PubMed]

Disclaimer/Publisher's Note: The statements, opinions and data contained in all publications are solely those of the individual author(s) and contributor(s) and not of MDPI and/or the editor(s). MDPI and/or the editor(s) disclaim responsibility for any injury to people or property resulting from any ideas, methods, instructions or products referred to in the content.